Energy & Environmental Science

Accepted Manuscript

ROYAL SOCIETY OF CHEMISTRY

www.rsc.org/ees

Energy & Environmental Science

RSCPublishing

PAPER

Full ceramic micro solid oxide fuel cells: Towards more reliable MEMS power generators operating at high temperatures

Cite this: DOI: 10.1039/xoxxoooooox

Received ooth January 2012,
Accepted ooth January 2012

DOI: 10.1039/xoxxoooooox

www.rsc.org/

I. Garbayo[a,b], D. Pla[a], A. Morata[a], L. Fonseca[b], N. Sabaté[b], A. Tarancón[a]

Batteries, with a limited capacity, have dominated the power supply of portable devices for decades. Recently, the emergence of new types of highly efficient miniaturized power generators like micro fuel cells has open alternatives for continuous operation on the basis of unlimited fuel feeding. This work addresses for the first time the development of a full ceramic micro solid oxide fuel cell fabricated in silicon technology. This full-ceramic device represents a new generation of miniaturized power generators able to operate at high temperatures, and therefore able to work with hydrocarbon fuel supply. Dense yttria-stabilized zirconia free-standing large-area membranes on micromachined silicon were used as electrolyte. Thin-film porous electrodes of $La_{0.6}Sr_{0.4}CoO_{3-\delta}$ and gadolinia-doped ceria were employed as cathode and anode materials, respectively. The electrochemical performance of all the components was evaluated by partial characterization using symmetrical cells and yielding excellent performance for the electrolyte (area specific resistance of 0.15 $\Omega \cdot cm^2$ at temperatures as low as 450ºC) and the electrodes (area specific resistance of the cathode and anode below 0.3 $\Omega \cdot cm^2$ at 700ºC). A micro solid oxide fuel cell with an active area of 2 mm^2 and less than 1 micrometer in thickness was characterized under fuel cell conditions, using hydrogen as a fuel and air as an oxidant. A maximum power density of 100 mW/cm^2 and 2 mW per single membrane was generated at 750ºC, having an open circuit voltage of 1.05 V. Impedance spectroscopy of the all-ceramic membrane showed a total area-specific resistance of ~3.5 $\Omega \cdot cm^2$.

Introduction

The energy gap between the capacity of the current battery technology and the power requirements of mobile devices is increasing year by year [1]. This energy divergence brings a new challenge on unlimited portable power generation that opens new opportunities for technologies beyond Li-ion batteries. In this new scenario, novel developments on the miniaturization of efficient power generators able to operate in continuous (by using a fuel) are receiving renewed attention. There is an increasing interest in micro Solid Oxide Fuel Cells (µSOFCs) fully integrated in silicon, especially after recent advances that make this disruptive technology a serious candidate to power next generations of portable devices [2].

In the last decade, several groups have presented promising

Broader context

Solid Oxide Fuel Cells (SOFC) are efficient electrochemical devices that convert chemical energy (in the form of fuel) into electricity. They are traditionally used for stationary power generation, but recent advances in their miniaturization have shown them as a promising alternative to current batteries for portable power supply. Micro SOFCs (µSOFC) have high energy density (up to x4 compared to Li-ion batteries) and instant refill capability, which will allow increasing the limited out-of-grid autonomy of current high performance devices. Moreover, µSOFC capability of working with hydrocarbon fuels is an advantage, due to their availability, easy handling, high specific energy and well-established regulations. Hydrocarbon reforming typically requires high temperatures above 600ºC. Imposing such temperatures on a µSOFC is feasible with low power consumption, by integrating its functional layers onto low thermal mass nanometric free-standing membranes. However, fast degradation of the state-of-the-art metallic electrodes takes place at those temperatures. Here, a full ceramic µSOFC is presented for the first time as a thermally stable system, up to 750ºC. Porous $La_{0.6}Sr_{0.4}CoO_{3-\delta}$ is used as cathode, dense yttria-stabilized zirconia as electrolyte and porous $Ce_{0.8}Gd_{0.2}O_{1.9-\delta}$ as anode. This work opens new insights for the development of a new generation of more reliable full ceramic µSOFC.

results on Si-integrated µSOFC systems. Evans et al. [3] reviewed in 2009 the main achievements of the different groups dealing with µSOFC, i.e. ETH Zurich [4,5], Stanford University [6–8], EPF Lausanne [9] and KIST [10]. Power outputs listed there ranged from values below 1 mW/cm^2 (ref. [9]) to a maximum of 861 mW/cm^2 at 450ºC using corrugated membranes (ref. [8]). Since then, main achievements prior to this work were carried out mainly by Prof. Ramanathan and co-workers at Harvard University [2,11–24], who published several articles showing power densities up to 1177 mW/cm^2 at 520ºC [21]. Table 1 updates and extends Evans' review by summarizing the complete series of power outputs (and corresponding fabrication parameters) published up to now on µSOFC devices based on functional free-standing membranes integrated in silicon [25–37].

The µSOFC operation temperatures covered in the literature are below T<560ºC (see Table 1 - Temp.). These low operation temperatures are beneficial from the materials point of view [38] but do not allow the integration of the cells into real systems fuelled with hydrocarbons, i.e. including a reformer unit (operation under pure hydrogen is out of consideration for portable applications for safety and practical reasons). Typical reforming reactors with the required high conversion and selectivity rates usually work at temperatures of ca. 700ºC [39–41]. Alternative conversion pathways, based on partial oxidation of hydrocarbons, have been recently proposed by Santis-Alvarez et al. [36,42,43] to reduce this high conversion temperature to T<600ºC. However, this promising route still requires a significant catalyst optimization to reach competitive performance compared to classical steam or dry reformers. The operation of a µSOFC at T>600ºC introduces new thermal stability needs for the self-supported electrolyte membranes and thin film electrodes.

About the membranes, the authors have recently reported the fabrication of thermo-mechanically resistant and defect-free large-area yttria-stabilized zirconia (YSZ) electrolyte membranes [44–46] stable up to 750ºC overcoming historically reported issues [47–49]. On the other hand, although poor stability of thin film metals like Pt above 400ºC has been extensively proved in bulky substrates [50–53], Pt continues being the material of choice for all the reported results for at least one of the electrodes of the µSOFC (see Table 1- Anode and Cathode). The quick degradation associated to dewetting processes and subsequent loss of performance have been even reported for µSOFCs [2,12,19], showing a rapid drop on the maximum power density after few hours of operation at temperatures as low as 500ºC (see Table 1 - Power stability). Presumably, this metal instability is also in the origin of the variability on the maximum power reported for analogous devices (see Table 1 - Power output). For example, Prinz et al. reported power values of 270 mW/cm^2 in 2007, 120 mW/cm^2 in 2009, 520 mW/cm^2 in 2011 and finally 198 mW/cm^2 in 2012, always using the same Pt/YSZ/Pt structure. A similar variability can be observed in Ramanathan et al.'s work (from ca. 30 mW/cm^2 in 2011 and 2012 to more than 1000 mW/cm^2 in 2012, although in this case the functional materials were slightly varied for each case) or Gauckler et al.'s publications (from 10 mW/cm^2 in 2008 to values above 150 mW/cm^2 in 2008 and 2012).

In order to address this big issue, more reliable electrodes are required (in fact, also for µSOFC operating at temperatures below 500ºC). By direct analogy with bulk SOFCs, ceramic-based electrodes would be the first choice. Several works have been recently published devoted to the development of pure oxide-based thin film cathodes [54–62]; however, only a few have focused on their implementation in µSOFC configurations (i.e. in free-standing membrane configurations) [13,14,31,63]. Among them, the authors have recently published the fabrication and integration of thin and porous $La_{0.6}Sr_{0.4}CoO_{3-\delta}$ (LSC) films into µSOFC devices showing area specific resistances of 0.3 Ω·cm^2 at 700ºC [64]. In contrast to this series of publications devoted to thin film cathodes, there is an alarming lack of works devoted to the development of thin film anodes, being Pt the only material tested up to now in µSOFC (with the only exception of Ramanathan and co-workers' work on the use of alternative metals Pd and Ru, see Table 1- Anode).

Two main strategies appear to be the most suitable for fabricating more reliable thin film anodes for µSOFC, namely (i.) the implementation of cermets based on stable ceramic scaffolds or (ii.) the use of more stable fully ceramic anode materials. Only a few works dealing with thin film cermet anodes (below 1 µm) have been published up to now [19,65–69], and among them, there is only one report on their implementation on µSOFC membranes [19]. Müller et al. prepared Ni-CGO by sol-gel chemistry observing quick conductivity degradation above 400ºC (see supplementary info of the reference [69]). Takagi et al. [19] fabricated a Ru-CGO composite observing a quite fast degradation of the so-fabricated µSOFC with time (62% of the initial power density within 3 h). From these results, it is clear that direct transferability of bulk SOFCs state-of-the-art anode materials is still a challenge for the thin film µSOFC community. On the other hand, it is well-known that pure ceramic electrodes typically used in bulk SOFCs do not present dewetting, thus being a promising alternative to metals for the anode side too (at higher operating temperatures). A recent publication by Jung et al. [65] has already shown the superior performance of columnar porous samarium-doped ceria (SDC) films for hydrogen electro-oxidation. This suggests columnar doped ceria as an excellent ceramic anode in the intermediate temperature regime, with no need of extra metallic component due to its high electronic conductivity under reducing conditions.

In this work, large-area self-supported membranes of YSZ ($(Y_2O_3)_{0.08}(ZrO_2)_{0.92}$) have been integrated in silicon microtechnology. Thin film porous electrodes were deposited on both sides of the membranes by using pulsed laser deposition (PLD). In particular, LSC was employed as a cathode and $Ce_{0.8}Gd_{0.2}O_{1.9-\delta}$ (CGO) as an anode. Microstructural characterization, in-plane conductivity measurements and electrochemical performance studies on both electrodes tested in symmetrical configuration have been carried out in order to determine their suitability for µSOFC integration. As an outcome, first results on device performance of a fully-ceramic based µSOFC are presented. The cell was evaluated under pure H_2 atmosphere at temperatures up to 750ºC.

Table 1 Comparison of previously reported results on μSOFC (*: corrugated membrane; power density calculated with respect to the projected area).

Group	Pub. year	Anode (dep. tech.)	Electrolyte (dep. tech.)	Cathode (dep. tech.)	PEN total thickness (nm)	Max. active area (mm^2)	OCV (V)	Power output ($mWcm^{-2}$)	Total power (mW)	Temp. (ºC)	Power stability	Ref.
Stanford Univ. (Prinz et al.)	2007	Pt (sp)	YSZ (sp)	Pt (sp)	80+50+80	0.01	1.05	130	0.013	350	-	6
		Pt (sp)	YSZ/GDC (sp)	Pt (sp)	80+100+80		1.10	200	0.020			
	2007	Pt (sp)	YSZ (ALD)	Pt (sp)	80+60+80	0.01	1.10	270	0.027	350	-	7
	2008	Pt (sp)	YSZ (ALD)	Pt (sp)	120+70+120	0.3 *	1.09	861 *	2.44	450	-	8
	2009	Pt (sp)	BYZ (ALD)	Pt (sp)	80+110+80	0.01	1.09	136	0.014	400	-	25
		Pt (sp)	BYZ (PLD)	Pt (sp)	80+130+80		1.12	120	0.012	450		
	2011	Pt (sp)	YSZ (ALD)	Pt (sp)	60+80+60	0.01*	1.11	560 820 *	0.056 0.082	450	-	27
	2011	Pt (sp)	YSZ (ALD)	Pt (sp)	120+70+120	4 (58.9%)	1.12	198	2.98	450	-	29
	2012	Pt (sp)	YSZ-YDC (ALD)	Pt (sp)	80+70+80	0.003	~1	1040	0.034	500	-	32
	2013	Pt (sp)	YSZ-YDC (ALD)	Pt (sp)	80+60+80	0.002*	1.05	1300 *	0.024	450	70% P_{max} ~ 1 h	33
ETH Zurich (Gauckler et al.)	2008	Pt (sp)	YSZ (PLD)	Pt (sp)	50+550+50		0.77	26	0.008			
		Pt (sp)	YSZ (PLD)	LSCF (s.pyr)	50+550+200	0.03	0.55	10	0.003	500	-	4
		Pt (sp)	YSZ (PLD)/YSZ (s.pyr)	Pt (paste)	50+750+10^4		1.06	150	0.045			
	2012	Pt (sp)	YSZ (PLD)/YSZ (s.pyr)	Pt (sp)	80+500+80	0.03	0.57	209	0.063	550	-	30
	2013	Pt (sp)	3YSZ (PLD)	LSC (s.pyr)	80+300+250	0.15	1.02	12	0.018	500	-	31
	2014	Pt (sp)	3YSZ (PLD)	Pt (sp)	60+300+60	0.15	1.07	47	0.070	565	-	36
ETH Zurich (Prestat et al.)	2013	Pt (sp)	YSZ (CVD)	Pt (sp)	80+100+80	0.13	0.84	166	0.22	410		34
			YSZ/CGO (CVD)		80+110+80		1.05	175	0.23	448		
EPFLausanne (Muralt et al.)	2008	Pt (sp)	YSZ (sp)	Pt (sp)	25+750+25	20 (with Ni grid)	0.28	-	-	400	-	9
	2010	Pt (sp)	YSZ (sp)	Pt (sp)	100+400+100	0.8(with Ni grid)	0.85	0.02	0.0002	500	-	26
Harvard Univ. (Ramanathan et al.)	2010	Pt (sp)	YSZ (sp)	LSCF (sp)	120+60+67	0.06	0.60	120	0.072	560	-	11
	2011	Pt (sp)	YSZ (sp)	Pt (sp)	80+100+80	0.03	0.97	1037	0.31	500	75% P_{max} < 1 h 50% P_{max} < 10 h	12
	2011	Pt (sp)	YSZ (sp)	BSCF (sp)	80+100+100	0.03	1.08	35	0.011	520	-	13
	2011	LSCF (sp)	YSZ (sp)	LSCF (sp)	65+60+65	0.03	0.18	0.21	0.00006	500	-	14
	2011	Pt (sp)	YSZ (sp)	LSCF (sp)	30+54+47	25 (with Ni grid)	0.75	155	21.1	510	86% P_{max} < 1 h 50% P_{max} < 10 h	2
	2011	Pd (sp)	YSZ (sp)	Pt (sp)	50+100+70	0.03	1.03	145	0.044	400	-	15
		Pd (sp)	YSZ (sp)	Pt (sp)			0.77	385 (with CH_4)	0.12	550		
	2011	Ru (sp)	YSZ (sp)	Pt (sp)	30+80+70	0.03	0.71	450 (with CH_4)	0.14	500	-	16
	2012	Pt (sp)	YSZ-CGO (sp)	Pt (sp)	80+100+80	0.03	0.41	1025	0.31	510	Stable OCV for > 50 h	17
		Pt (sp)	YSZ/YSZ-CGO (sp)	Pt (sp)	80+120+80		0.73	930	0.28			
	2012	Pt (sp)	ZrO_2 (sp)	Pt (sp)	55+50+55	0.03	0.91	33	0.010	450	-	18
	2012	Ru-CGO (sp)	YSZ (sp)	Pt (sp)	30+100+40	0.04	0.99	275 (with CH_4)	0.11	485	62% P_{max} in 3 h	19
	2012	Pt (sp) VO_x/Pt (sp) VO_x (sp)	YSZ (sp)	Pt (sp)	25+95+25	0.02	~1 ~1 ~ 0.75	~10 6.6 ~1	0.002 0.001 0.0002	360	-	20
	2012	Pt (sp) Pt (sp) Ru (sp)	CGO/YSZ (sp)	Pt (sp)	n/a+85+n/a	0.03	0.6 0.95 0.85	1177 412 665 (with CH_4)	0.30 0.11 0.17	520	-	21
	2013	Ru (sp)	YSZ (sp)	Pt (sp)	50+110+70	0.04	0.92	440 (with CH_4)	0.18	500	-	22
		Ru (sp)	YSZ (sp)	Pt (sp)			0.96	410 (with nat.gas)	0.16			
	2013	Pt (sp)	YSZ (sp)	Pt (sp)	n/a+100+n/a	0.03	~1	108 (with CH_4)	0.028	405	-	23
	2013	Pt (sp)	YDC (sp)	Pt (sp)	n/a+100+n/a	0.03	~1	125	0.032	500	-	24
	2014	Pt (sp)	YSZ (sp)	Pt (sp)	n/a+100+n/a	3.14	0.87	75	~3	500	-	37
KIST (Son et al.)	2011	Pt (sp)	YSZ (PLD)	Pt (sp)	80+200+80	0.01	1.06	-	-	400	-	28
		Pt on AAO (sp)	YSZ (PLD)	Pt (sp)	80+900+80		1.02	350	0.035	500		
	2014	Pt (sp)	BCY/BZY (PLD)	Pt (sp)	100+200+100	0.02	0.98	145	0.029	400	Abrupt decrease in OCV	35
This work	**2014**	**CGO (PLD)**	**YSZ (PLD)**	**LSC (PLD)**	**250+300+200**	**1.90**	**1.10**	**100**	**1.90**	**750**	-	-

Experimental

Large-area self-supported electrolyte membranes integrated in silicon microtechnology

The fabrication of free-standing low-thermal mass large-area membranes is described in detail in references [70–72], and is briefly summarized in Figure 1. In order to increase the active free-standing area of the device, the total area was enlarged by using a grid of doped-silicon slabs as mechanical support. A photolithographic step in the first stage of the microfabrication flow was used to define certain zones to be doped on the initial silicon wafer (see Figure 1a). Since heavily p-doped silicon is not affected by anisotropic etchants used in silicon micromachining [73], these regions define the future supporting slabs. After doping, a SiO_2/Si_3N_4 dielectric bilayer was deposited on both sides of the wafers (Figure 1b). Then, by selectively etching the Si substrate from the backside, large area Si_3N_4 free-standing membranes were released on the topside of the Si wafer (reinforced by the non-etched doped silicon slabs). These membranes were then used as a substrate for the electrolyte deposition, carried out by means of PLD using previously reported conditions [44,45] (Figure 1c-d). Afterwards, the electrolyte free-standing membranes were released, by removing the remaining silicon nitride layer from the backside using reactive ion etching (RIE) (Figure 1e). Once obtained the free-standing electrolyte membrane, the electrodes were deposited on both sides (cathode topside, Figure 1f, and anode backside, Figure 1g). For the final measurements, patterned metallic dense films were additionally implemented on both sides of the tri-layer ceramic membrane by nanosphere lithography [64,72], serving as current collectors.

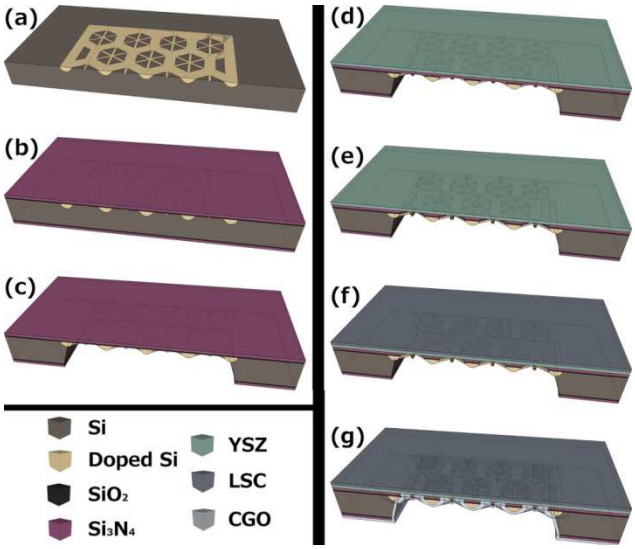

Fig. 1 Main steps of the fabrication process flow of large-area µSOFC self-supported membranes.

Thin film functional layers deposition and characterization

Porous CGO and LSC thin film electrodes (anode and cathode, respectively) were deposited by PLD on top of previously deposited dense YSZ thin electrolyte films. The whole series of depositions were carried out on a PLD5000 equipment from PVD Products, which allows the deposition of functional layers at a wafer level (4" substrates). Deposition conditions for YSZ and LSC were adapted from previous works already published by the authors on the development and optimization of these materials for µSOFC electrolyte [44–46] and cathode [64], respectively. Meanwhile, the fabrication and characterization of ceria-based anode films for µSOFC were specifically developed in this work.

Electrode/electrolyte bilayers were first deposited on $Si_3N_4/SiO_2/Si$ bulk substrates for their microstructural and in-plane electrochemical characterization (this particular study is presented as supplementary information). A porosity control (from full density in the electrolyte to high porosity in the electrodes) was accomplished by changing the background pressure on the deposition chamber, from 0.025 mbar for the YSZ to 0.13 mbar for either CGO or LSC. The deposition temperature employed for YSZ was 600ºC while 100ºC for the electrode films. The growing rates for the different functional layers were found to be ~2.5 nm YSZ/min (wafer level deposition, laser energy 0.75 J/cm^2 at 10 Hz), ~10 nm CGO/min (small area deposition, laser energy 0.5 J/cm^2 at 10 Hz) and ~3.2 nm LSC/min (small area deposition, laser energy 0.3 J/cm^2 at 20 Hz). Scanning electron microscopy (SEM, Zeiss Auriga) was used for the study of the microstructure of all the deposited films. Cross-sectional images were always taken from fractured samples.

The performance of the here developed CGO anode was tested under real µSOFC operating conditions by fabricating symmetrical CGO/YSZ/CGO free-standing membranes. Optical microscopy (Nikon Eclipse ME600) was used to check membranes state during the fabrication process. Half-cell measurements were performed under single 5% H_2 – 95% Ar reducing atmospheres and the electrochemical response of the thin film anode was characterized by impedance spectroscopy (EIS). The electrochemical characterization was carried out on a Probostat cell inside a high temperature furnace. Pt current collectors were deposited by sputtering (Alcatel A610 sputtering equipment at p_{Ar}=0.01 mbar, P=100 W and ν_{RF}=13.6 MHz). EIS across the membrane was performed by applying small AC voltages of 50 mV in order to keep the linear regime at the measurement temperature range, in the frequency range from 30 MHz to 0.1 Hz (Novocontrol Alpha-A frequency analyzer with ZG4 test interface). Measurements were performed at temperatures between 150ºC and 700ºC using heating/cooling rates of 5ºC/min, in order to properly separate the contribution of each component of the cell from the total resistance.

Fabrication and characterization of full ceramic µSOFC membranes

Full ceramic-based free-standing membranes were fabricated by using the materials previously developed and studied as either the electrolyte (dense YSZ), anode (porous CGO) or cathode (porous LSC) thin films. Pt-based current collectors were also added on both sides of the membrane. The size of the silicon chips containing single large-area membranes was

10x10 mm^2. The final µSOFC structure was Pt/LSC/YSZ/CGO/Pt and Table 2 summarizes the main fabrication parameters used for each functional layer in this work.

In order to measure the fuel cell performance, samples were sealed to an alumina tube by using an Ag O-ring and heated up to 750ºC (5ºC/min). Pure Ar was fed to the anode for sealing, while synthetic air was employed at the cathode side. Once the sample was properly sealed, pure H_2 was introduced in the anode side. Open circuit voltage (OCV) of the cell was measured on galvanostatic mode by applying a negligible current flow between the electrodes and measuring the generated voltage using a Keithley 2400 sourcemeter. Once an OCV close to the theoretical one was obtained, Intensity-Voltage (I-V) curves were performed on galvanostatic mode, again by means of a Keithley 2400 sourcemeter. Finally, EIS experiments were complementarily carried out on the measured membranes in order to evaluate the associated resistance to each component of the fully ceramic-based µSOFC (frequency range from 30 MHz to 0.1 Hz (Novocontrol Alpha-A frequency analyzer with ZG4 test interface)).

Results and discussion

Fabrication and characterization of large-area self-supported YSZ membranes as µSOFC electrolytes

Self-supported membranes of Si_3N_4 were successfully fabricated by silicon micromachining. PLD deposition of YSZ and subsequent RIE etching of the Si_3N_4 layer were carried out to fabricate and release the YSZ membranes. Figure 2 shows top and bottom views of the typically obtained self-supported large-area electrolyte membranes, and a real image of the fabricated Si-based devices. Although other membrane sizes were fabricated in the same wafer (with a total area ranging from 2.20 mm^2 up to 11.30 mm^2), in this work, the evaluated membranes have a total area of 2.50 mm^2 for an *active* area (only YSZ free-standing area) of 1.90 mm^2. This represents an enhancement of *ca.* 20x over previously reported basic squared free-standing membrane configurations [3]. The buckling patterns observed in the free-standing part of the membranes (see Figure 2a) correspond to a compressive strain introduced by atomic impingement during the PLD deposition together with the TEC difference between the YSZ layer and the silicon substrate. This strain field is required for avoiding membrane break during thermomechanical cycling since the silicon substrate tightens the membrane during the heating step. Further details on the origin and thermomechanical response of the so-strained membranes can be found on references [44,45]. This capability of fabricating thermally stable YSZ membranes at intermediate-to-high operation temperatures (up to 800ºC) is the cornerstone for the integration of ceramic electrodes presented here for the first time.

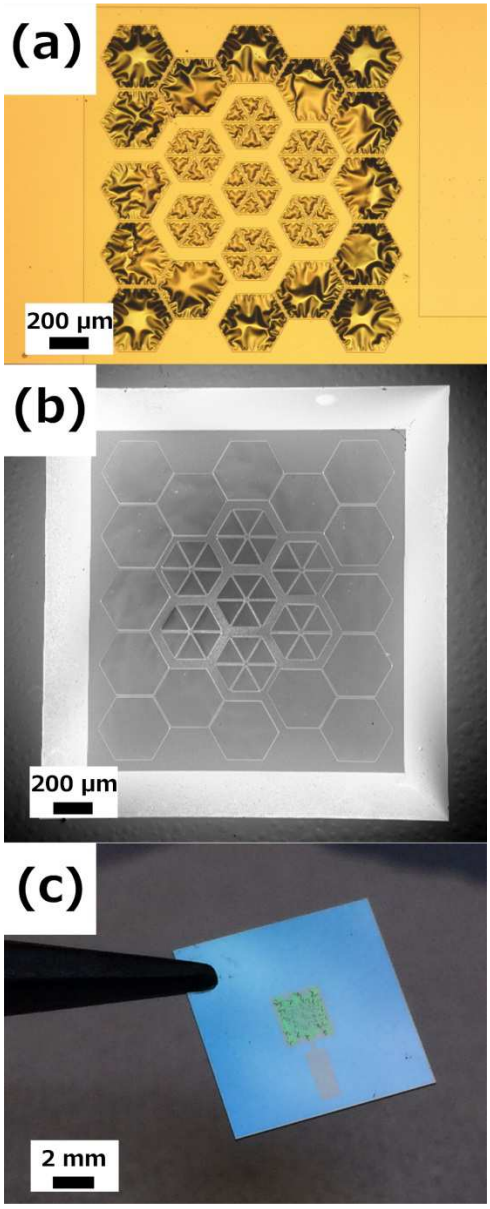

Fig. 2 (a,b) Top view (optical image) and bottom view (SEM image) of a large-area free-standing membrane (already including the electrodes and current collectors). (c) Real image of one of the fabricated free-standing membranes supported on a Si-based substrate.

Table 2 Materials and main fabrication parameters used for the fabrication of full ceramic-based µSOFC (RT = room temperature).

	Material	Deposition technique	Deposition temperature	Microstructure	Film thickness
Curr. collector	Pt	Sputtering	RT	Dense patterned	150 nm
Cathode	$La_{0.6}Sr_{0.4}CoO_{3-\delta}$	PLD	100ºC	Porous	200 nm
Electrolyte	$(Y_2O_3)_{0.08}(ZrO_2)_{0.92}$	PLD	600ºC	Dense	300 nm
Anode	$Ce_{0.8}Gd_{0.2}O_{1.9-\delta}$	PLD	100ºC	Porous	250 nm

As shown in Figure 3, large-area membranes exhibited values of conductivity similar to those previously reported for basic square membranes (where the maximum area achievable was limited to ca. 0.5 mm^2) [45] and also for bulk YSZ [74]. These results confirm the reproducibility of the fabrication of large-area YSZ membranes, maintaining the exceptional electrochemical performance achieved with smaller membranes. The typically ascribed target value for the Area specific resistance of SOFC electrolytes (ASR = 0.15 $\Omega \cdot cm^2$, [75]) was reached at temperatures as low as 450ºC (for <300 nm-thick YSZ films), proving the fabricated YSZ membranes as an excellent electrolyte on the whole range of intermediate temperatures (450ºC<T<800ºC).

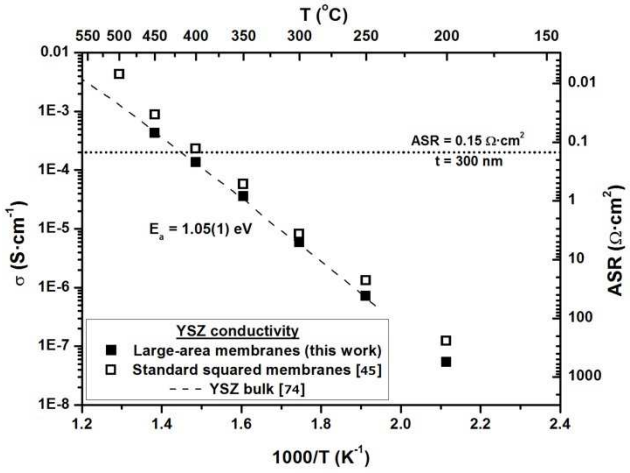

Fig. 3 Arrhenius plot of cross-plane electrical conductivity of large-area YSZ membranes. Previously reported values for YSZ conductivity measured on standard squared membranes [45] and also bulk YSZ conductivity [74] are also included for comparison. Values of area specific resistance (ASR) plotted on right Y axis are calculated for 300 nm-thick YSZ films.

Electrochemical characterization of thin film porous electrodes

Porous LSC thin films as a cathode for µSOFC. Porous LSC thin film layers were deposited by PLD directly on the self-supported YSZ electrolyte membranes. Details of the optimization of the deposition and performance of the LSC layer in µSOFC configurations can be found elsewhere in a recent work published by the authors [64]. SEM images (top view and cross-section) of a porous LSC layer fabricated by PLD on top of dense YSZ after annealing up to operating temperatures, i.e. 700ºC, can be also found in Figure S1 (Electronic Supplementary Information). As shown in ref. [64], the in-plane conductivity of the so fabricated LSC layer is the one expected for the bulk material (σ(700ºC)~200 $S \cdot cm^{-1}$) while the commonly accepted Area Specific Resistance target for SOFC electrode/electrolyte bilayers (ASR=0.30 Ωcm^2, [75]) is achieved at 700ºC indicating the optimum temperature of operation.

Porous CGO thin films as an anode for µSOFC. As presented in the Electronic Supplementary Information file (Figures S2 to S5), an optimization of the PLD deposition conditions and post-annealing treatment was carried out for CGO films in order to ensure good crystallinity and enough porosity. A columnar and well-ordered grain growth similar to the YSZ electrolyte and LSC cathode films was observed for the CGO layer (see Figure S3). The formation of this type of microstructure was driven by a high background pressure during the PLD deposition that increases the mobility of species on the ablation plume and allows the formation of separated clusters that generates a porous network [76]. In-plane conductivity measurements carried out by using the Van der Pauw method yielded values comparable to the ones reported in the literature for CGO under reducing conditions [77] (σ=0.04 S/cm at 700ºC, see Figure S6). Despite this low conductivity, a negligible resistance associated to the current from the reaction point to the collector (typically few micrometers away in µSOFC configurations) is expected. This short distance to be covered by the current, characteristic of µSOFCs, allows employing materials previously discarded for bulk SOFCs due to a low conductivity.

The CGO thin film anodes were then implemented on free-standing membranes and tested under real µSOFC conditions. Figure 4 shows the as fabricated CGO/YSZ/CGO symmetrical free-standing membranes including patterned dense Pt current collectors. Cross-sectional SEM images with different magnification of the same membrane are presented in the figure. A similar microstructure than the one obtained on bulk substrates was observed (i.e. porous and columnar CGO films and highly dense and columnar YSZ film, see Figure S3). Film homogeneity was excellent along the whole free-standing membrane. YSZ films of 300 nm and CGO of 250 nm are complemented with dense patterned 150 nm-thick Pt films on both sides of the membrane for a total thickness of ca. 1 µm. The obtained membranes showed the same typical buckling pattern already observed on the YSZ membranes (see Figure 2a) indicating a negligible strain contribution of the porous anode film to the field of strains from the YSZ membrane itself. Therefore, the overall mechanical behaviour will be still controlled by the electrolyte.

Figure 5 depicts a Nyquist plot corresponding to the impedance spectrum obtained for a symmetrical membrane at 650ºC, under a reducing atmosphere (5% H_2 - 95% Ar). Two separated arcs were clearly observed with resistance values of the same order of magnitude, but clearly separated due to the difference on their associated capacitance, i.e. time constant. The data was fitted according to the equivalent circuit depicted on the inlet of Figure 5 (R_s corresponds to a series resistance; $R_{HF}Q_{HF}$ and $R_{LF}Q_{LF}$ correspond to the in-parallel resistor-capacitor elements associated to the high frequency and low frequency arcs, respectively). Resistance and capacitance values calculated for each artefact appeared on the Nyquist plots are collected in Table 3. Values from the high frequency and low frequency arcs are normalized to the membrane active area. True capacitances are calculated from the constant phase elements used for fitting according to ref. [78].

It is important to notice here that the contribution from the dense YSZ electrolyte is expected to be negligible at such temperatures, as shown in previous studies on the same type of substrates [45] and in Figure 3. Therefore, the series resistance is totally associated to the

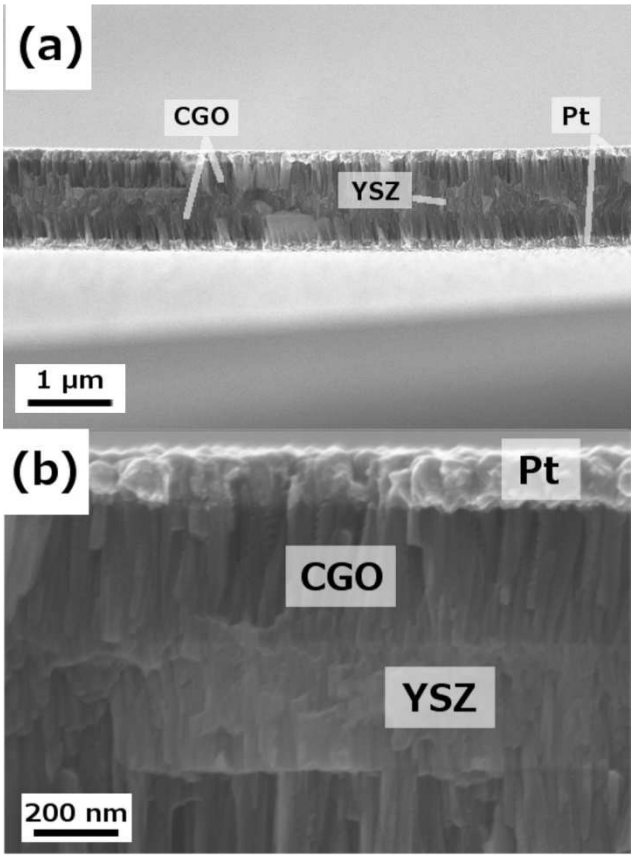

Fig. 4 Different magnification cross-sectional SEM images of a Pt/CGO/YSZ/CGO/Pt free-standing membrane, after thermal treatment at 700ºC.

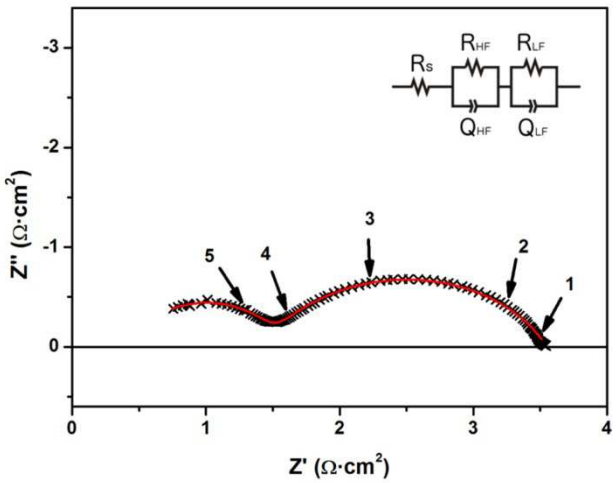

Fig. 5 Impedance spectra of a symmetrical Pt/CGO/YSZ/CGO/Pt membrane, measured at T=650ºC. Solid red line represents the fitting using the equivalent circuit depicted. The numbers refer to the frequency decades covered by the EIS analysis.

current collection and cable resistances. The two arcs observed in the spectrum can be associated to the CGO electrode. True capacitances measured for the high frequency (CHF = 10-6 F/cm2) and low frequency (CLF = 10-4 F/cm2) arcs suggest a correspondence between (i.) the HF-arc and the oxygen transport/diffusion in the CGO electrode; and (ii.) the LF-arc and the electrochemical reaction for the oxidation of hydrogen at the ceria surface. The appearance of high frequency arcs with resistances associated to the transport of ions across grain boundaries has been extensively reported for composite electrodes based on CGO with characteristic capacitances of the order of magnitude here reported, i.e. C = 10-6 F/cm2, [79,80]. Since similar values of capacitance are also expected for a double-layer capacitance formed between CGO and YSZ [81], the resistance associated to the HF-arc could be alternatively associated to the oxygen transport through the electrode-electrolyte interface. Coming back to the low-frequency arc, the obtained large capacitance exceeding the typical values for electrochemical reactions at planar surfaces ($C=10^{-3}$ F/cm^2) reinforces the idea of a CGO working as a MIEC, i.e. extending the active surface to the bulk. A simple calculation of the surface extension achieved by using a columnar CGO like the one presented here yields a 20- to 50-fold increase of the active area. Therefore, the larger values of capacitance obtained seem reasonable and are in good agreement with previously reported columnar samaria-doped ceria [65]. The MIEC behaviour observed in the impedance spectra also illustrates that Pt layers deposited on top are simply acting as current collectors, while the CGO is playing the electrode role.

Figure 6 shows an Arrhenius plot of the Area Specific Resistance corresponding to the high frequency (ASR_{HF}) and low frequency (ASR_{LF}) arcs as a function of the temperature. In both cases, the ASR dependence on temperature follows an Arrhenius-type law, with activation energies of E_a = 0.9 eV and E_a = 1.5 eV, respectively. Activation energies around 0.8 – 1.0 eV were previously reported for oxide-ion conduction on CGO films [82] while activation energies of the order of 1.5 eV or higher were reported for thin film MIECs in the literature [38,57,66,83–85]. This correlation reinforces the association proposed on the basis of the impedance spectrum analysis indicating that the CGO is fully acting as the electrode in the symmetrical cells.

Table 3 ASR and capacitance values calculated for each artefact appeared on the Nyquist plots of a symmetrical Pt/CGO/YSZ/CGO/Pt membrane, measured from T=400ºC to T=650ºC by EIS.

T (ºC)	R_s (Ω)	High Frequency (HF) arc				Low Frequency (LF) arc			
		ASR (Ωcm^2)	Q (F/cm^2)	n	C (F/cm^2)	ASR (Ωcm^2)	Q (F/cm^2)	n	C (F/cm^2)
650	23	0.50	$3.5\cdot10^{-6}$	0.88	$6.6\cdot10^{-7}$	1.0	$1.2\cdot10^{-3}$	0.73	$1.3\cdot10^{-4}$
600	23	1.1	$3.8\cdot10^{-6}$	0.84	$4.1\cdot10^{-7}$	1.6	$5.9\cdot10^{-4}$	0.78	$1.1\cdot10^{-4}$
550	29	1.7	$2.7\cdot10^{-6}$	0.85	$3.4\cdot10^{-7}$	4.6	$8.4\cdot10^{-4}$	0.72	$1.2\cdot10^{-4}$
500	27	2.8	$2.3\cdot10^{-6}$	0.85	$3.1\cdot10^{-7}$	18	$1.3\cdot10^{-3}$	0.61	$2.0\cdot10^{-4}$
450	25	6.6	$1.9\cdot10^{-6}$	0.86	$3.4\cdot10^{-7}$	130	$8.6\cdot10^{-4}$	0.59	$3.0\cdot10^{-4}$
400	30	19	$1.2\cdot10^{-6}$	0.89	$3.5\cdot10^{-7}$	370	$4.0\cdot10^{-4}$	0.58	$1.7\cdot10^{-4}$

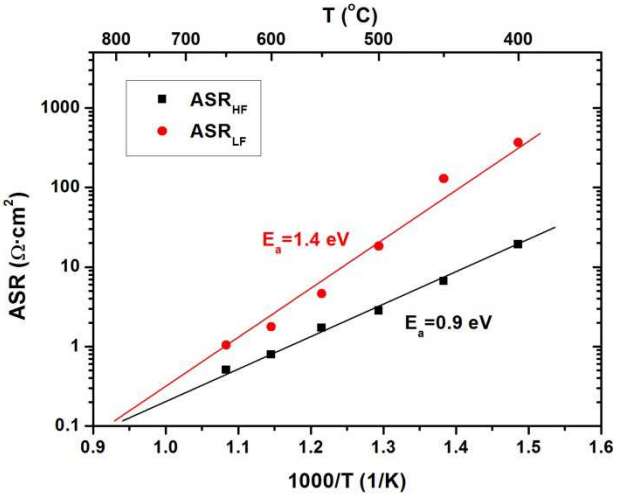

Fig. 6 Temperature evolution of the ASR of the two artefacts appearing on the EIS analysis of symmetrical Pt/CGO/YSZ/CGO/Pt free-standing membranes, i.e. high frequency arc (HF) and low frequency arc (LF).

As shown in Figure 6, polarization resistances are in good agreement with the ones reported by Jung et al. [65] for similar SDC films at the same temperature (ASR=5.73 Ωcm^2 at 650ºC for Jung's 220 nm thick layers) indicating the possibility of integrating the CGO as an anode in a real µSOFC structure without performance loses. In particular, target values of ASR for anode/electrolyte interfaces in SOFCs (ASR=0.30 Ωcm^2, [75]) were attained at temperatures of ca. 700ºC. Since this temperature is similar to the one obtained for the target ASR in LSC/YSZ [64], a full ceramic µSOFC based on CGO as anode, YSZ as electrolyte and LSC as cathode is shown to be totally feasible.

Fabrication and characterization of full ceramic-based µSOFC

Highly buckled membranes were obtained after cathode and anode deposition (see Figure 2a) due to the clearly dominating compressive strain of the YSZ free-standing films [44,45]. No change on the buckling pattern was observed suggesting a negligible stress contribution of the two porous electrodes. Figure 7 shows cross-sectional view images of the fabricated large-area µSOFC. The different microstructure of each layer can be distinguished in the cross-sectional SEM image. High porosity was observed on both LSC (top) and CGO (bottom) electrodes, while high density and packed columnar grains arrangements were evident for the YSZ electrolyte. Pt current collectors were implemented at both sides of the functional tri-layer. The µSOFC membranes were found to be stable under operating conditions since no cracks appeared after thermal cycling up to 750ºC. Similar microstructures than those observed on post-annealed thin films deposited over bulk substrates (see Figures S1 and S3c-d on the Electronic Supplementary Information file) and half-cell measurements (see Figure 4 for the anode and reference [64] for the cathode) were observed on the final full ceramic µSOFC after testing at 750ºC. Even ultra-rapid thermal cycling was successfully

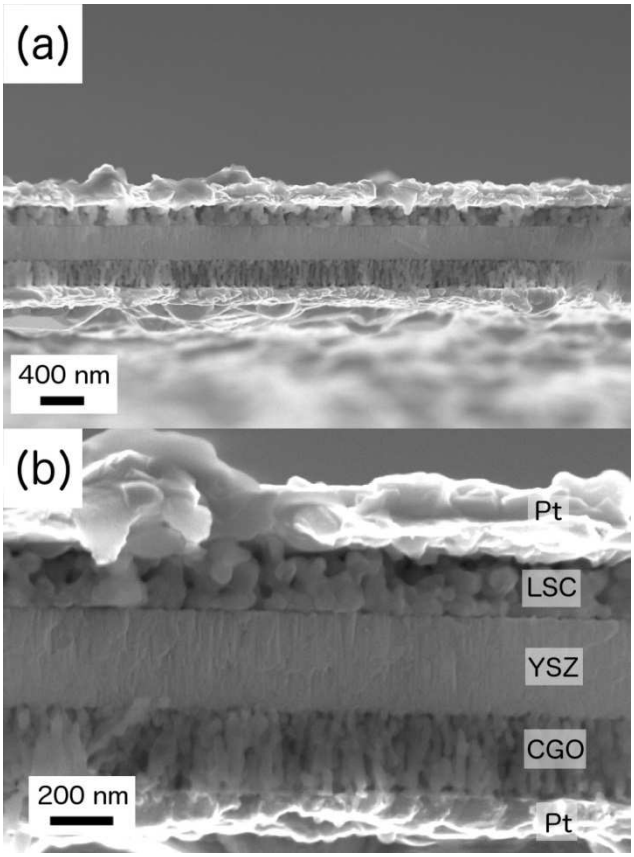

Fig. 7 Different magnification cross-sectional SEM images of a Pt/LSC/YSZ/CGO/Pt free-standing membrane, after measuring at 750ºC.

applied, as shown in the video file included in the supplementary information.

As shown in Figure 7, the free-standing µSOFC was ca. 1 µm thick (including the Pt current collectors). The functional cathode/electrolyte/anode ceramic tri-layer showed a total thickness of ca. 750 nm, with an electrolyte of 300 nm. Despite thinner electrolyte layers were commonly employed in the past, even by the authors [45], in this work the thickness of the YSZ layer was increased. An electrolyte thickness of several hundreds of nanometres enhances its reliability without affecting the electrochemical performance. Thicker electrolyte layers (deposited in two stages with a cleaning step in between) reduce the formation of through-pinholes and increase the thermomechanical stability of the membrane while keeping a negligible associated resistance at the operation temperature. For an electrolyte of 300 nm the area specific resistance can be as low as 0.15 Ωcm^2 at temperatures below 450ºC (see Figure 3). Considering electrodes operating at 700ºC like in this case, even thicker electrolyte than the one employed here will not limit the µSOFC performance.

Figure 8 shows I-V curves obtained for one of the measured Pt/LSC/YSZ/CGO/Pt free-standing membranes at different temperatures, up to 800ºC[†]. An Open Circuit Voltage (OCV) close to the theoretical value was obtained once sealed (OCV = 1.05 V), using synthetic air as oxidizing atmosphere (cathode side) and pure H_2 as reducing atmosphere (anode side). Although specific long-term tests have to be done, these values

of OCV together with stable power densities were maintained for more than 5h at the operating temperatures (T=700-750ºC, see Figure S7), thus ensuring the reliability of the membranes from an electrochemical point of view, i.e. no pinholes or cracks appeared on the membranes during heating up, sealing and measuring. The importance of sealing problems and leakages due to pinhole formation can be clearly observed in the wide range of reported OCVs for different μSOFCs (see Table 1 - OCV), some of them far away from the theoretical value (~ 1.1 V) [2,4,9,11,14,17,30]. The power output was calculated as a function of the current density, showing a maximum value of 100 mW/cm^2 at 750ºC and 65 mW/cm^2 at 700ºC. The total power output extracted from a single cell was ca. 2 mW at 750ºC, which is in the upper range of power per cell previously reported for μSOFCs (see Table 1 - Total Power). These power output values are in the typical range for bulk SOFC and metallic-based μSOFCs (see Table 1 - Power Output) being a clear proof-of-concept of the feasibility of a full-ceramic μSOFC operating at the required high temperatures.

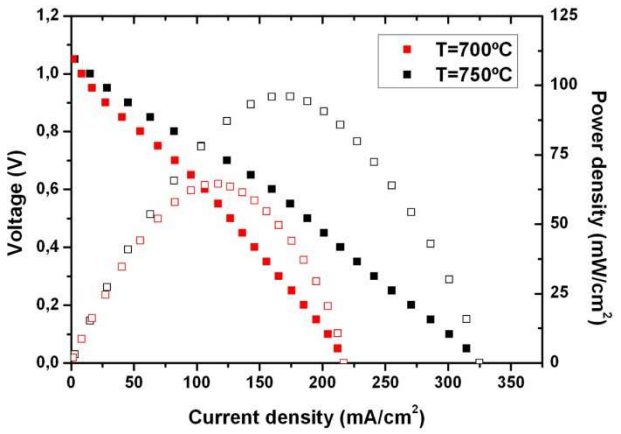

Fig. 8 I-V curve (closed symbols) and power density output (open symbols) obtained from a Pt/LSC/YSZ/CGO/Pt free-standing membrane at 700ºC and 750ºC.

Figure 9 shows a Nyquist plot corresponding to a Pt/LSC/YSZ/CGO/Pt free-standing membrane at 750ºC under high power output (applied bias of 0.7 V). Since, at least, two separated arcs can be identified in the plot, an equivalent circuit $R_s(R_{HF}Q_{HF})(R_{LF}Q_{LF})$ was proposed. The series resistance R_s includes the resistances associated to the YSZ electrolyte, the Pt current collectors and the cables and contacts. Values of R_s of several ohms were measured (see a detail of the high frequency range in the insert of Figure 9) mainly corresponding to the current collector and cable resistances (as commented before and according to previous studies [45], a 300 nm-thick YSZ film at T > 700ºC presents a negligible resistance of ca. 10^{-6} Ω·cm^2). The arcs observed in the plot can be associated to the two electrodes of the μSOFC. High frequency and low frequency arcs present resistance values of the same order of magnitude (see listed values on Table 4) with associated capacitances of C_{HF} = 10^{-6} F/cm^2 and C_{LF} = 10^{-3} F/cm^2. These values of capacitance suggest a double contribution from the different phenomena involved in both electrodes, i.e. capacitances associated to oxide ion transport (likely in the CGO anode) and non-charge transfer phenomena typical of high surface active areas of a MIEC (in the CGO anode and the LSC cathode). It is important to notice here that no significant effect of Si diffusion in the electrolyte or electrode films was observed in this work (see Figure S8), neither LSC-YSZ interdiffusion reactions [64]. Since the series resistance contribution is negligible in comparison with the total resistance of the cell, the thin film ceramic electrodes represents the main source of resistance loses in the cell. The high frequency arc associated to the oxide-ion transport inside the CGO electrode and the low frequency arc corresponding to the electrochemical reactions represent almost half-half of the total resistance (ASR=1.5 Ω·cm^2 and 2.0 Ω·cm^2, respectively). These values of ASR are one order of magnitude higher than the expected from symmetrical cell measurements (either for CGO or LSC films) indicating that the integration of both ceramic electrodes in the μSOFC requires further optimization. On-going work is being devoted to explore different alternatives to reduce the anode and cathode polarization resistances, and especially the resistance associated to the oxide-ion transport through the porous CGO film.

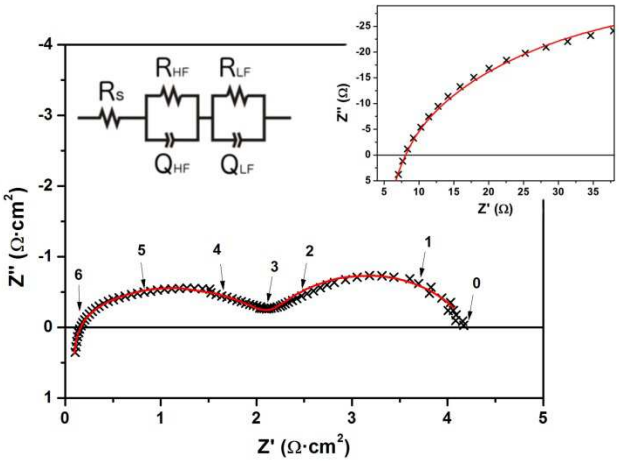

Fig. 9 Nyquist plot of a Pt/LSC/YSZ/CGO/Pt free-standing membrane at 750ºC and voltage offset of 0.7 V. The inlet shows a zoom of the high frequency part of the plots. Solid red line represents the fitting using the equivalent circuit depicted. The numbers refer to the frequency decades covered by the EIS analysis.

Table 4 ASR values calculated for each artefact appeared on the Nyquist plot of a Pt/LSC/YSZ/CGO/Pt membrane at 750ºC and voltage offset of 0.7 V (c.c.: current collectors).

	BIAS: 0.7 V	
	ASR (Ωcm^2)	C (F/cm^2)
High frequency arc	1.5	$1 \cdot 10^{-6}$
Low frequency arc	2.0	$3 \cdot 10^{-3}$
Electrolyte + c.c.	< 0.02	-

Summing up, the goal of fabricating reliable large-area μSOFCs able to operate at temperatures above 700ºC is addressed here for the first time on the basis of durable ceramic

electrodes and robust self-suspended YSZ membranes. Figure 10 shows a plot of the total power per single µSOFC versus power density and operating temperature published by different authors, compared to this work (based on Table 1). The novel strategy for increasing the active area above 2mm^2, i.e. high power per unit cell (>2mW), overcomes the limits presented by most of the published devices (with total power below 100µW) while operating at temperatures 200ºC higher. Since the stability of the employed ceramic electrodes is out of discussion (stability tests of the independent electrodes in thin film form carried out in the past, i.e. references [64,65]; see also Figure S9 on the Electronic Supplementary Information), the realization of this full ceramic µSOFC reinforces the feasibility of this technology and opens a new avenue in the implementation of novel strategies for improving the power density to competitive values above 500 mW/cm^2. Also, although the reproducibility and thermomechanical stability of the whole ceramic membrane is ensured, specific long-term tests will be carried out as the ultimate study of reliability of the here-reported full ceramic µSOFC.

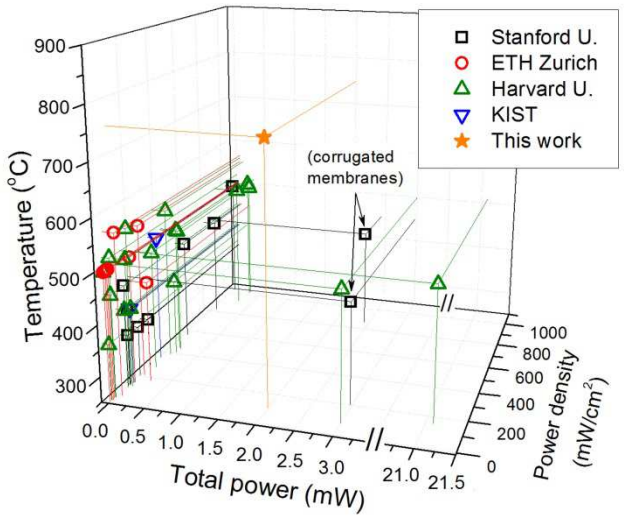

Fig. 10 Representation of the state-of-the-art in µSOFC in terms of total power per single device, power density obtained and operating temperature.

Conclusions

A full ceramic-based µSOFC has been presented here for the first time, opening a new family of robust µSOFCs able to operate at high temperature (where hydrocarbon reforming can be considered for fuelling). Large-area (> 2mm^2) free-standing µSOFCs were fabricated using a porous LSC thin film as cathode, a dense membrane of YSZ as electrolyte and a porous CGO thin film as anode. The thermo-mechanical stability of the µSOFC membrane was proved up to 750ºC, thus extending the up-to-now reported operating temperatures of µSOFC (< 550ºC). Pure ceramic cathode and anode films showed good electrochemical performance in real µSOFC configurations at temperatures of 700ºC (ASR<0.30 Ω·cm^2). Measurements of the fuel cell performance of the device were carried out at 700 – 750ºC. A maximum power density of 100 mW/cm^2 was measured at 750ºC, under pure H_2 as a fuel and synthetic air as an oxidant, for a total power per cell of 2 mW. Therefore, a new generation of more reliable µSOFCs, based on ceramics, is presented in this work as a promising candidate for a real implementation of these miniaturized MEMS power generators in portable devices.

Acknowledgements

This investigation has been supported by the Spanish Ministry of Economy and Competitiveness (Consolider MULTICAT CDS-2009-00050, POWER PACK ENE2010-14833, MAT-2008-04931 and TEC-2009-14660-C02-01 projects), the "Generalitat de Catalunya" (Advanced Materials for Energy Network, XaRMAE, 2009-SGR-00050). Part of this study was funded by the European Institute of Innovation and Technology (KIC Innoenergy, Electric Energy and Storage Project). The research was also supported by European Regional Development Funds (ERDF, FEDER Programa Competitivitat de Catalunya 2007e2013). AT and NS would like to thank the financial support of the Ramon y Cajal postdoctoral program. The authors would like to particularly thank Dr. Mónica Burriel and Prof. John Kilner for SIMS measurements presented in the Electronic Supplementary Information file.

Notes and references

[a] IREC, Catalonia Institute for Energy Research, Dept of Advanced Materials for Energy Applications. Jardí de les Dones de Negre 1, 2nd Floor, 08930 Sant Adrià del Besòs, Barcelona, Spain.
[b] IMB-CNM (CSIC), Institute of Microelectronics of Barcelona - National Microelectronics Center, CSIC. Campus UAB, 08193 Bellaterra, Barcelona, Spain.

† Measurements below 650ºC showed insufficient performance (no electrode activation), and tests at higher temperatures (T ≥ 800ºC) yielded to membrane failure (similar thermomechanical limits were previously reported by the authors [45]).

Electronic Supplementary Information (ESI) available: Additional details on the microstructural optimization of porous LSC and CGO films as well as a comparison of the thermal stability of different thin film electrodes can be found on the ESI file. Moreover, open circuit voltage and power density evolution of the cell with time during the test is included. Finally, a video showing the thermomechanical stability of the presented µSOFC under ultra-rapid thermal cycling is provided. See DOI: 10.1039/b000000x/

1. S. B. Schaevitz, in *Proc. of SPIE*, 2012, p. 824802.
2. M. Tsuchiya, B.-K. Lai, and S. Ramanathan, *Nat Nano*, 2011, **6**, 282–286.
3. A. Evans, A. Bieberle-Hütter, J. L. M. Rupp, and L. J. Gauckler, *J. Power Sources*, 2009, **194**, 119–129.

4. U. P. Muecke, D. Beckel, A. Bernard, A. Bieberle-Hütter, S. Graf, A. Infortuna, P. Müller, J. L. M. Rupp, J. Schneider, and L. J. Gauckler, *Adv. Funct. Mater.*, 2008, **18**, 3158–3168.
5. A. Bieberle-Hütter, D. Beckel, A. Infortuna, U. P. Muecke, J. L. M. Rupp, L. J. Gauckler, S. Rey-Mermet, P. Muralt, N. R. Bieri, N. Hotz, M. J. Stutz, D. Poulikakos, P. Heeb, P. Müller, A. Bernard, R. Gmür, and T. Hocker, *J. Power Sources*, 2008, **177**, 123–130.
6. H. Huang, M. Nakamura, P. Su, R. Fasching, Y. Saito, and F. B. Prinz, *J. Electrochem. Soc.*, 2007, **154**, B20–B24.
7. J. H. Shim, C.-C. Chao, H. Huang, and F. B. Prinz, *Chem. Mater.*, 2007, **19**, 3850–3854.
8. P.-C. Su, C.-C. Chao, J. H. Shim, R. Fasching, and F. B. Prinz, *Nano Lett.*, 2008, **8**, 2289–2292.
9. S. Rey-Mermet and P. Muralt, *Solid State Ionics*, 2008, **179**, 1497–1500.
10. C.-W. Kwon, J.-W. Son, D.-J. Lee, K.-B. Kim, J.-H. Lee, and H.-W. Lee, in *European Fuel Cell Forum*, Lucerne, 2008, p. B0519.
11. B.-K. Lai, K. Kerman, and S. Ramanathan, *J. Power Sources*, 2010, **195**, 5185–5196.
12. K. Kerman, B.-K. Lai, and S. Ramanathan, *J. Power Sources*, 2011, **196**, 2608–2614.
13. K. Kerman, B.-K. Lai, and S. Ramanathan, *J. Power Sources*, 2011, **196**, 6214–6218.
14. B.-K. Lai, K. Kerman, and S. Ramanathan, *J. Power Sources*, 2011, **196**, 1826–1832.
15. B.-K. Lai, K. Kerman, and S. Ramanathan, *J. Power Sources*, 2011, **196**, 6299–6304.
16. Y. Takagi, B.-K. Lai, K. Kerman, and S. Ramanathan, *Energy Environ. Sci.*, 2011, **4**, 3473–3478.
17. K. Kerman, B.-K. Lai, and S. Ramanathan, *J. Power Sources*, 2012, **202**, 120–125.
18. C. Ko, K. Kerman, and S. Ramanathan, *J. Power Sources*, 2012, **213**, 343–349.
19. Y. Takagi, S. Adam, and S. Ramanathan, *J. Power Sources*, 2012, **217**, 543–553.
20. Q. Van Overmeere, K. Kerman, and S. Ramanathan, *Nano Lett.*, 2012, **12**, 3756–3760.
21. K. Kerman, B.-K. Lai, and S. Ramanathan, *Adv. Energy Mater.*, 2012, **2**, 656–661.
22. Y. Takagi, K. Kerman, C. Ko, and S. Ramanathan, *J. Power Sources*, 2013, **243**, 1–9.
23. K. Kerman, T. Tallinen, S. Ramanathan, and L. Mahadevan, *J. Power Sources*, 2013, **222**, 359–366.
24. K. Kerman, Q. Van Overmeere, M. Karpelson, R. J. Wood, and S. Ramanathan, *ACS Nano*, 2013, **7**, 10895–10903.
25. J. H. Shim, J. S. Park, J. An, T. M. Gür, S. Kang, and F. B. Prinz, *Chem. Mater.*, 2009, **21**, 3290–3296.
26. S. Rey-Mermet, Y. Yan, C. Sandu, G. Deng, and P. Muralt, *Thin Solid Films*, 2010, **518**, 4743–4746.
27. C.-C. Chao, C.-M. Hsu, Y. Cui, and F. B. Prinz, *ACS Nano*, 2011, **5**, 5692–5696.
28. C.-W. Kwon, J.-W. Son, J.-H. Lee, H.-M. Kim, H.-W. Lee, and K.-B. Kim, *Adv. Funct. Mater.*, 2011, **21**, 1154–1159.
29. P.-C. Su and F. B. Prinz, *Electrochem. commun.*, 2012, **16**, 77–79.
30. R. Tölke, A. Bieberle-Hütter, A. Evans, J. L. M. Rupp, and L. J. Gauckler, *J. Eur. Ceram. Soc.*, 2012, **32**, 3229–3238.
31. A. Evans, C. Benel, A. J. Darbandi, H. Hahn, J. Martynczuk, L. J. Gauckler, and M. Prestat, *Fuel Cells*, 2013, **13**, 441–444.
32. Z. Fan, J. An, A. Iancu, and F. B. Prinz, *J. Power Sources*, 2012, **218**, 187–191.
33. J. An, Y.-B. Kim, J. Park, T. M. Gür, and F. B. Prinz, *Nano Lett.*, 2013, **13**, 4551–4555.
34. M. V. F. Schlupp, A. Evans, J. Martynczuk, and M. Prestat, *Adv. Energy Mater.*, 2013, DOI: 10.1002/aenm.201301383.
35. K. Bae, D. Y. Jang, H. J. Jung, J. W. Kim, J.-W. Son, and J. H. Shim, *J. Power Sources*, 2014, **248**, 1163–1169.
36. B. Scherrer, A. Evans, A. J. Santis-Alvarez, B. Jiang, J. Martynczuk, H. Galinski, M. Nabavi, M. Prestat, R. Tölke, A. Bieberle-Hütter, D. Poulikakos, P. Muralt, P. Niedermann, A. Dommann, T. Maeder, P. Heeb, V. Straessle, C. Muller, and L. J. Gauckler, *J. Power Sources*, 2014.
37. K. Kerman, S. Xuza, and S. Ramanathan, *J. Electroceramics*, 2014.
38. A. Tarancón, *Energies*, 2009, **2**, 1130–1150.
39. A. Bieberle-Hutter, A. J. Santis-Alvarez, B. Jiang, P. Heeb, T. Maeder, M. Nabavi, D. Poulikakos, P. Niedermann, A. Dommann, P. Muralt, A. Bernard, and L. J. Gauckler, *Lab Chip*, 2012, **12**, 4894–4902.
40. B. T. Schädel, M. Duisberg, and O. Deutschmann, *Catal. Today*, 2009, **142**, 42–51.
41. N. J. Divins, E. López, Á. Rodríguez, D. Vega, and J. Llorca, *Chem. Eng. Process. Process Intensif.*, 2013, **64**, 31–37.
42. A. J. Santis-Alvarez, M. Nabavi, B. Jiang, T. Maeder, P. Muralt, and D. Poulikakos, *Chem. Eng. Sci.*, 2012, **84**, 469–478.
43. A. J. Santis-Alvarez, R. Büchel, N. Hild, W. J. Stark, and D. Poulikakos, *Appl. Catal. A Gen.*, 2014, **469**, 275–283.
44. A. Tarancón, N. Sabaté, A. Cavallaro, I. Gràcia, J. Roqueta, I. Garbayo, J. P. Esquivel, G. Garcia, C. Cané, and J. Santiso, *J. Nanosci. Nanotechnol.*, 2010, **10**, 1327–1337.
45. I. Garbayo, A. Tarancón, J. Santiso, F. Peiró, E. Alarcón-LLadó, A. Cavallaro, I. Gràcia, C. Cané, and N. Sabaté, *Solid State Ionics*, 2010, **181**, 322–331.
46. I. Garbayo, G. Dezanneau, C. Bogicevic, J. Santiso, I. Gràcia, N. Sabaté, and A. Tarancón, *Solid State Ionics*, 2012, **216**, 64–68.
47. C. D. Baertsch, K. F. Jensen, J. L. Hertz, H. L. Tuller, S. T. Vengallatore, S. M. Spearing, and M. A. Schmidt, *J. Mater. Res.*, 2004, **19**, 2604–2615.
48. D. J. Quinn, M.Sc. Thesis, Massachusetts Institute of Technology, 2006.
49. N. Yamamoto, M.Sc. Thesis, Massachusetts Institute of Technology, 2006.
50. T. Ryll, H. Galinski, L. Schlagenhauf, P. Elser, J. L. M. Rupp, A. Bieberle-Hutter, and L. J. Gauckler, *Adv. Funct. Mater.*, 2011, **21**, 565–572.
51. H. Galinski, T. Ryll, L. Schlagenhauf, L. J. Gauckler, P. Stender, and G. Schmitz, *Phys. Rev. B*, 2012, **85**, 125408.
52. X. Wang, H. Huang, T. Holme, X. Tian, and F. B. Prinz, *J. Power Sources*, 2008, **175**, 75–81.

53. H. Galinski, T. Ryll, P. Elser, J. L. M. Rupp, A. Bieberle-Hütter, and L. J. Gauckler, *Phys. Rev. B*, 2010, **82**, 235415.
54. H.-I. Ji, J. Hwang, K. J. Yoon, J.-W. Son, B.-K. Kim, H.-W. Lee, and J.-H. Lee, *Energy Environ. Sci.*, 2013, **6**, 116–120.
55. P. Plonczak, A. Bieberle-Hütter, M. Søgaard, T. Ryll, J. Martynczuk, P. V. Hendriksen, and L. J. Gauckler, *Adv. Funct. Mater.*, 2011, **21**, 2764–2775.
56. C. Benel, A. J. Darbandi, R. Djenadic, A. Evans, R. Tölke, M. Prestat, and H. Hahn, *J. Power Sources*, 2013, **229**, 258–264.
57. J. Hayd, L. Dieterle, U. Guntow, D. Gerthsen, and E. Ivers-Tiffée, *J. Power Sources*, 2011, **196**, 7263–7270.
58. J. Hayd, H. Yokokawa, and E. Ivers-Tiffée, *J. Electrochem. Soc.*, 2013, **160**, F351–F359.
59. N. I. Karageorgakis, A. Heel, A. Bieberle-Hütter, J. L. M. Rupp, T. Graule, and L. J. Gauckler, *J. Power Sources*, 2010, **195**, 8152–8161.
60. C. Peters, A. Weber, and E. Ivers-Tiffée, *J. Electrochem. Soc.*, 2008, **155**, B730–B737.
61. F. S. Baumann, J. Maier, and J. Fleig, *Solid State Ionics*, 2008, **179**, 1198–1204.
62. P. Plonczak, D. R. Sørensen, M. Søgaard, V. Esposito, and P. V. Hendriksen, *Solid State Ionics*, 2012, **217**, 54–61.
63. A. C. Johnson, B.-K. Lai, H. Xiong, and S. Ramanathan, *J. Power Sources*, 2009, **186**, 252–260.
64. I. Garbayo, V. Esposito, S. Sanna, A. Morata, D. Pla, L. Fonseca, N. Sabaté, and A. Tarancón, *J. Power Sources*, 2014, **248**, 1042–1049.
65. W. Jung, J. O. Dereux, W. C. Chueh, Y. Hao, and S. M. Haile, *Energy Environ. Sci.*, 2012, **5**, 8682–8689.
66. U. P. Muecke, K. Akiba, A. Infortuna, T. Salkus, N. V Stus, and L. J. Gauckler, *Solid State Ionics*, 2008, **178**, 1762–1768.
67. G. La O, J. Hertz, H. Tuller, and Y. Shao-Horn, *J. Electroceramics*, 2004, **13**, 691–695.
68. J. L. Hertz and H. L. Tuller, *J. Electrochem. Soc.*, 2007, **154**, B413–B418.
69. G. Müller, R.-N. Vannier, A. Ringuedé, C. Laberty-Robert, and C. Sanchez, *J. Mater. Chem. A*, 2013, **1**, 10753.
70. ES Patent, 2012, P201230973.
71. M. Salleras, I. Garbayo, C. Calaza, A. Tarancón, I. Gràcia, L. Fonseca, C. Cané, J. Santiso, and N. Sabaté, in *Power MEMS*, Leuven, 2010, pp. 215–218.
72. I. Garbayo, M. Salleras, A. Tarancón, A. Morata, G. Sauthier, J. Santiso, and N. Sabaté, in *10th European SOFC Forum*, Luzern, 2012, vol. 6 - A07, pp. A07 – 38–44.
73. L. Fonseca, J. Santander, R. Rubio, N. Sabaté, E. Figueras, M. Duch, I. Gràcia, and C. Cané, *Sensors Actuators B Chem.*, 2008, **130**, 538–545.
74. J. B. Goodenough, *Annu. Rev. Mater. Res.*, 2003, **33**, 91–128.
75. N. P. Brandon, S. Skinner, and B. C. H. Steele, *Annu. Rev. Mater. Res.*, 2003, **33**, 183–213.
76. A. Infortuna, A. S. Harvey, and L. J. Gauckler, *Adv. Funct. Mater.*, 2008, **18**, 127–135.
77. C. Kleinlogel, *Solid State Ionics*, 2000, **135**, 567–573.
78. J. Fleig, *Solid State Ionics*, 2002, **150**, 181–193.
79. S. Primdahl and Y. L. Liu, *J. Electrochem. Soc.* , 2002, **149** , A1466–A1472.
80. E. Perry Murray, *Solid State Ionics*, 2001, **143**, 265–273.
81. N. L. Robertson and J. N. Michaels, *J. Electrochem. Soc.* , 1991, **138** , 1494–1499.
82. H. Inaba and H. Tagawa, *Solid State Ionics*, 1996, **83**, 1–16.
83. F. S. Baumann, J. Fleig, H. U. Habermeier, and J. Maier, *Solid State Ionics*, 2006, **177**, 3187–3191.
84. P. Plonczak, M. Søgaard, A. Bieberle-Hütter, P. V. Hendriksen, and L. J. Gauckler, *J. Electrochem. Soc.*, 2012, **159**, B471–B482.
85. J. Fleig, *Annu. Rev. Mater. Res.*, 2003, **33**, 361–382.

Full ceramic micro solid oxide fuel cells: Towards more reliable MEMS power generators operating at high temperatures

I. Garbayo, D. Pla, A. Morata, L. Fonseca, N. Sabaté, A. Tarancón

- ELECTRONIC SUPPLEMENTARY INFORMATION -

In-plane microstructural and electrochemical characterization of porous LSC films

The particular study of porous LSC films deposited by PLD for their use as cathodes in Si-integrated µSOFC is reported in reference [64] (in the main manuscript). Here, top and cross section views of one of the fabricated LSC cathodes are also included, for easy finding.

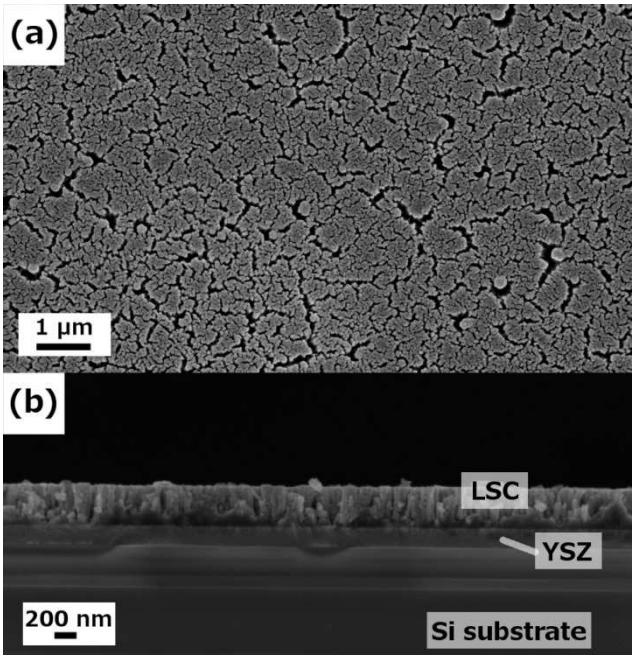

Fig. S1 Top view (a) and cross-sectional view (b) SEM images of a porous LSC cathode layer deposited by PLD, after thermal treatment up to 700ºC.

In-plane microstructural and electrochemical characterization of porous CGO films

The microstructural study was made by scanning electron microscopy (SEM) on a Zeiss Auriga equipment. The evolution of the microstructure with temperature was characterized by imaging samples before and after thermal treatments up to μSOFC operating temperatures (T=700ºC). In addition, phase identification and its evolution with temperature was made by means of in-situ X-ray diffraction (XRD) on a Brucker-D8 Advance equipment. Data acquisition was performed every 50ºC for studying pattern evolution while heating up.

In order to evaluate the electronic conductivity of the thin CGO, in-plane conductivity measurements were carried out on as-deposited porous CGO films (250 nm thick), by using the Van der Pauw technique. Four gold electrodes were defined on top of the CGO films (close to the corner edges) for their use as electrical contacts. Measurements were carried out at different temperatures from 25ºC to 700ºC by means of a Keithley 2400 sourcemeter, on a Probostat cell placed inside a furnace and using slow heating and cooling ramps ($1ºC \cdot min^{-1}$). As intended to be used as anode, a reducing atmosphere based on 5% H_2 – 95% Ar mixture was fed inside the furnace.

Figure S2 shows the evolution with temperature of the XRD pattern of a CGO/YSZ bilayer deposited over bulk $Si/SiO_2/Si_3N_4$ substrates, where the spectrum marked as RT (room temperature) corresponds to the as-deposited sample and consecutive annealing temperatures are shown, from 400ºC to 700ºC. Diffraction peaks from both crystalline YSZ and CGO diffraction patterns (cubic Fm-3m structure from JCPDS-ICDD #30-1468 and #75-0161, respectively) were already observed on as-deposited samples, despite having been prepared with very different conditions, i.e. 100ºC for the CGO and 600ºC for the YSZ. As expected since deposited at high temperatures, YSZ layer was fully crystalline as-deposited and no peak evolution was observed when heating up to 700ºC. However, sharper and more intense peaks were observed for the CGO when increasing the temperature (see the increment on T_a on Figure S2). This observation points to the crystallization of a certain amount of the amorphous CGO expected to be present in the as-deposited films due to the lower deposition temperature. In terms of fabrication, this improvement on crystallinity at such intermediate temperatures is considered very convenient. More crystalline films are expected to present better electrochemical performance, due to the improvement on mass transport properties of the crystallites compared to the amorphous form.

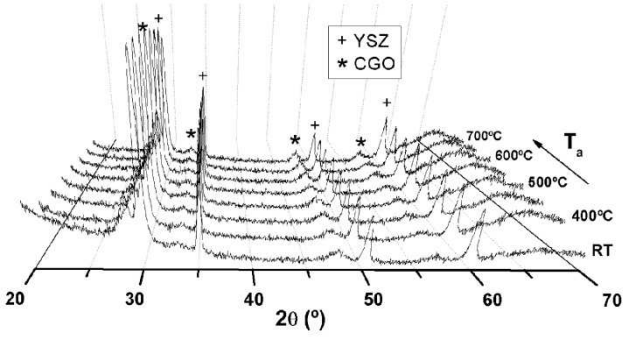

Fig. S2 X-Ray diffraction patterns of a porous CGO film deposited over dense YSZ on a $Si_3N_4/SiO_2/Si$ substrate, measured at different annealing temperatures (T_a).

Figure S3 shows top view and cross-section SEM images of as-deposited (a,b) and post-annealed at 700ºC for 5 h (c,d) CGO porous layers deposited over dense YSZ films, as complementary microstructural study to the XRD experiment. The experiment was carried out under reducing atmospheres (5% H_2-95% Ar), using heating/cooling rates of 5ºC/min. No significant differences were observed on the YSZ film before and after the thermal treatment, showing a great stability with temperature (consistent with previous XRD observations). Meanwhile, more faceted grains were observed on the CGO film and a much more open porosity was attained (see Figure S3c). The crystallization of the partially amorphous CGO is probably the reason for the microstructural change promoted by temperature, and it is considered to be beneficial for the electrode performance as it facilitates the diffusion of gas species through it.

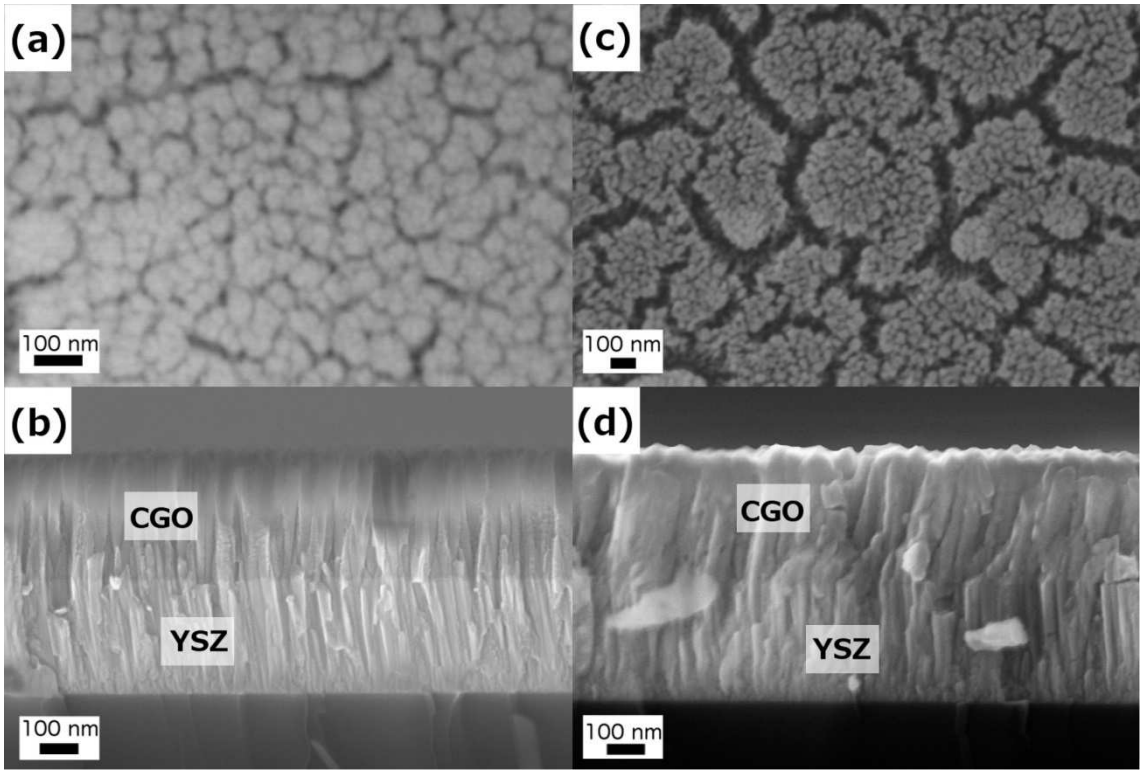

Fig. S3 Top view and cross-section SEM images of as-deposited (a,b) and post-annealed (c,d) 250 nm-thick porous CGO layers over previously deposited dense YSZ.

As can be observed in Figure S4, good step coverage was found on the backside of the wafer when depositing the porous CGO anode. This was possible due to (i.) the typical step profile generated by anisotropic etching the Si with KOH (following the 111 planes, i.e. 54º versus the substrate surface, which was 100-oriented), and (ii.) the relatively high thickness of the CGO films deposited in this work (t>200 nm) which ensured a good coverage.

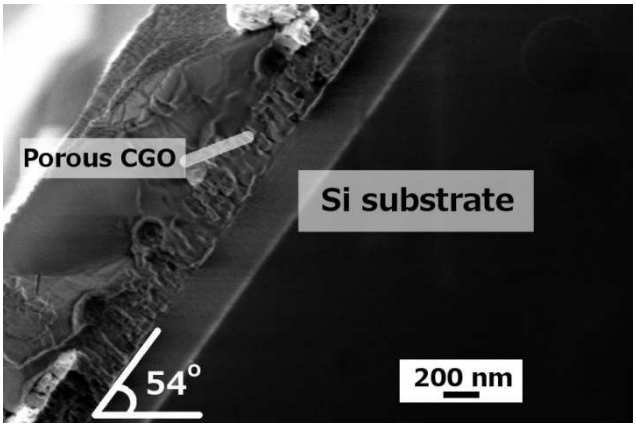

Fig. S4 Cross-section SEM image of the porous CGO anode showing the covering of the backside tilted profile (54º) on the Si-based supporting platform.

Porous CGO films of both 250 nm and 1 µm thick were fabricated, for testing the maximum thickness achievable while remaining thermomechanically stable. Problems of detachment and cracking appeared under operating conditions (T=700ºC) on the thicker films, while the thinner ones remained stable. Figure S5 shows top view and cross-sectional images of a 1 µm-thick CGO/YSZ bilayer delaminated from the Si-based substrate after thermal treatment, opposed to the 250 nm-thick films shown in Figure S3 (c,d). Maximum CGO thickness for fabricating reliable thin film CGO/YSZ bilayers was therefore limited to less than 1 µm.

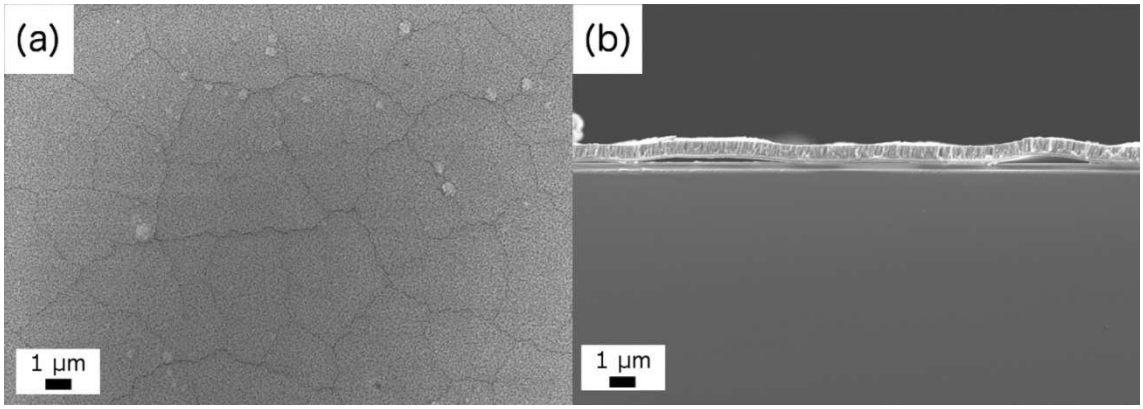

Fig. S5 Top view and cross-section SEM images showing delamination when increasing CGO thickness up to 1 µm.

Figure S6 shows an Arrhenius plot of the CGO conductivity as a function of temperature. As expected, low conductivity values (less than 0.1 S/cm) were measured on the porous films in the whole range of operating temperatures, i.e. up to 700ºC. Although still showing the anode functionality of the fabricated CGO films, that low conductivity was clearly insufficient for current percolation. Therefore, for effectiveness of porous CGO thin film anodes, adding an electronic conductor element on top (current collector) was definitely needed, reducing as much as possible the distance between the reaction points and the collector.

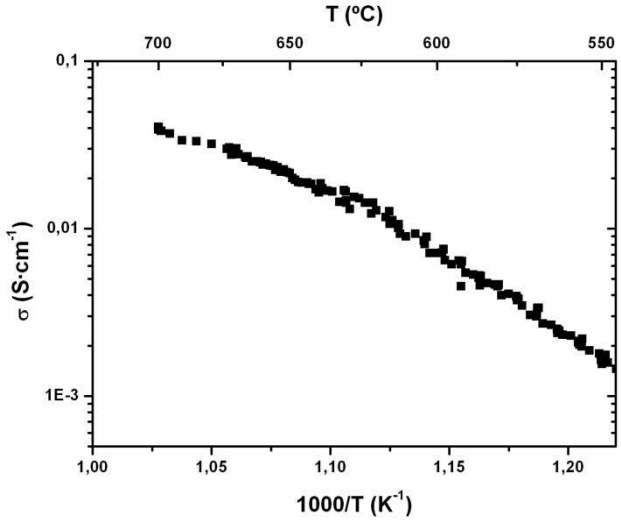

Fig. S6 Evolution of the in-plane conductivity of a 250 nm-thick porous CGO anode deposited over dense YSZ on a $Si_3N_4/SiO_2/Si$ substrate, measured by the van der Pauw method.

Thin film electrolyte chemical composition

The chemical composition used in this work for the electrolyte was 8YSZ ($(Y_2O_3)_{0.08}(ZrO_2)_{0.92}$). According to a previous publication by the authors (reference [46] in the main text), 3YSZ ($(Y_2O_3)_{0.08}(ZrO_2)_{0.92}$) would be however a better choice, mainly due to the better mechanical properties of the PLD targets and the corresponding reduction of particle ejection.

In this work, we used a large-area PLD equipment in order to develop an industrial process (able to carry out depositions at a wafer-level). Unfortunately, the unavailability of a proper 3YSZ target (prepared by SPS as suggested in the cited reference) for its use in large area PLD forced us to use 8YSZ instead. Despite this, the new equipment presents a 60º angle configuration (vs. the typical 45º) that greatly reduces the presence of particulates in the membranes. In addition, a double deposition process (with a cleaning step in the middle) was also implemented with the same objective. Finally, the results (although following a more cumbersome process) were comparable to the ones employing 3YSZ SPS targets.

Open Circuit Voltage and power density evolution of the µSOFC during the test experiment

Figure S7 shows the evolution of the open circuit voltage (OCV) of the cell and the power density at V=0.7V during the test experiment. As shown in the figure, an OCV close to the theoretical one (OCV>1.0V) was obtained after heating up to 700ºC and sealing during *ca.* 2h at such temperature (Ag O-ring was used for this purpose). After that, the cell was heated up to 750ºC and the OCV was maintained at ~1.05V for more than 2.5 h. No drop of OCV was observed during that time. Stable values of power density around P~85mW/cm^2 were maintained during dwelling time at 750ºC. At t=460min (>7.5h), the cell was heated up to 800ºC, showing membrane failure and final drop of the OCV.

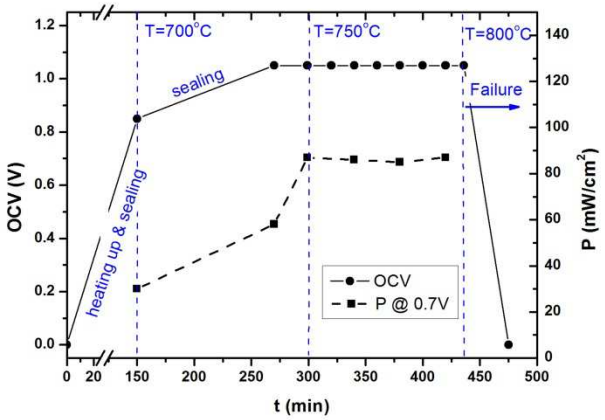

Fig. S7 Evolution of the Open Circuit Voltage (OCV) and power density at V=0.7V (P) of the µSOFC during the test experiment.

Disambiguation of the possible silicon diffusion through thin functional films deposited over Si-based substrates

Silicon diffusion into YSZ is a potential problem in thin film μSOFCs based on silicon technology, since it blocks the ionic conductivity by increasing the grain boundary resistance (where Si accumulates). Although previous studies have shown a negligible grain boundary contribution to the total resistance of YSZ membranes in silicon platforms, for this study, SIMS depth profiling carried out at the Imperial College London (in collaboration with Dr. M. Burriel and Prof. J. Kilner) showed that Si does not diffuse at 800ºC through the YSZ layer (see Figure S8).

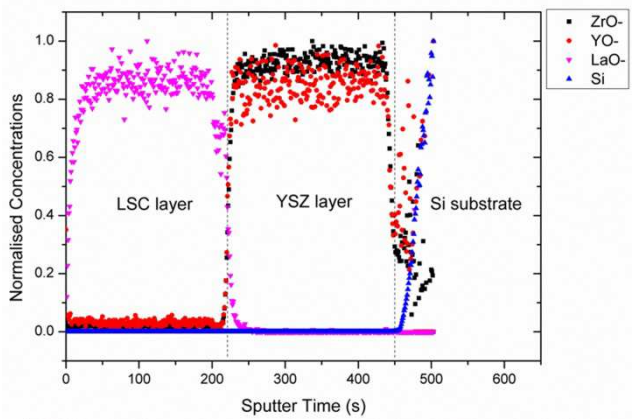

Fig. S8 SIMS depth profile coming from a LSC/YSZ thin film bilayer deposited on a $Si_3N_4/SiO_2/Si$ substrate, similar to the ones used for the μSOFC fabrication.

Electrode microstructural stability under operating conditions – Comparison with thin film Pt electrodes

Figure S9 shows top view SEM images of the here-fabricated electrodes, before and after thermal treatment at 700ºC for >10h, compared to one of the traditional metallic electrodes used on Pt/YSZ/Pt μSOFC configurations. The images are taken on thin film electrodes deposited over YSZ electrolytes on bulk Si-based substrates ($Si_3N_4/SiO_2/Si$). Oxidizing atmosphere (synthetic air) were used on LSC and Pt electrodes thermal treatments, while a reducing atmosphere (5% H_2-95% Ar) was used for the CGO anode. As it can be observed, the ceramic nanostructure remains stable with temperature (porous but continuous layer) while the Pt drastically agglomerates from starting dense layers (room temperature) into isolated particles after annealing, thus losing the electrode performance (breakdown of in-plane percolation). A similar behaviour was observed on the Pt films when annealing under reducing atmospheres (not shown here).

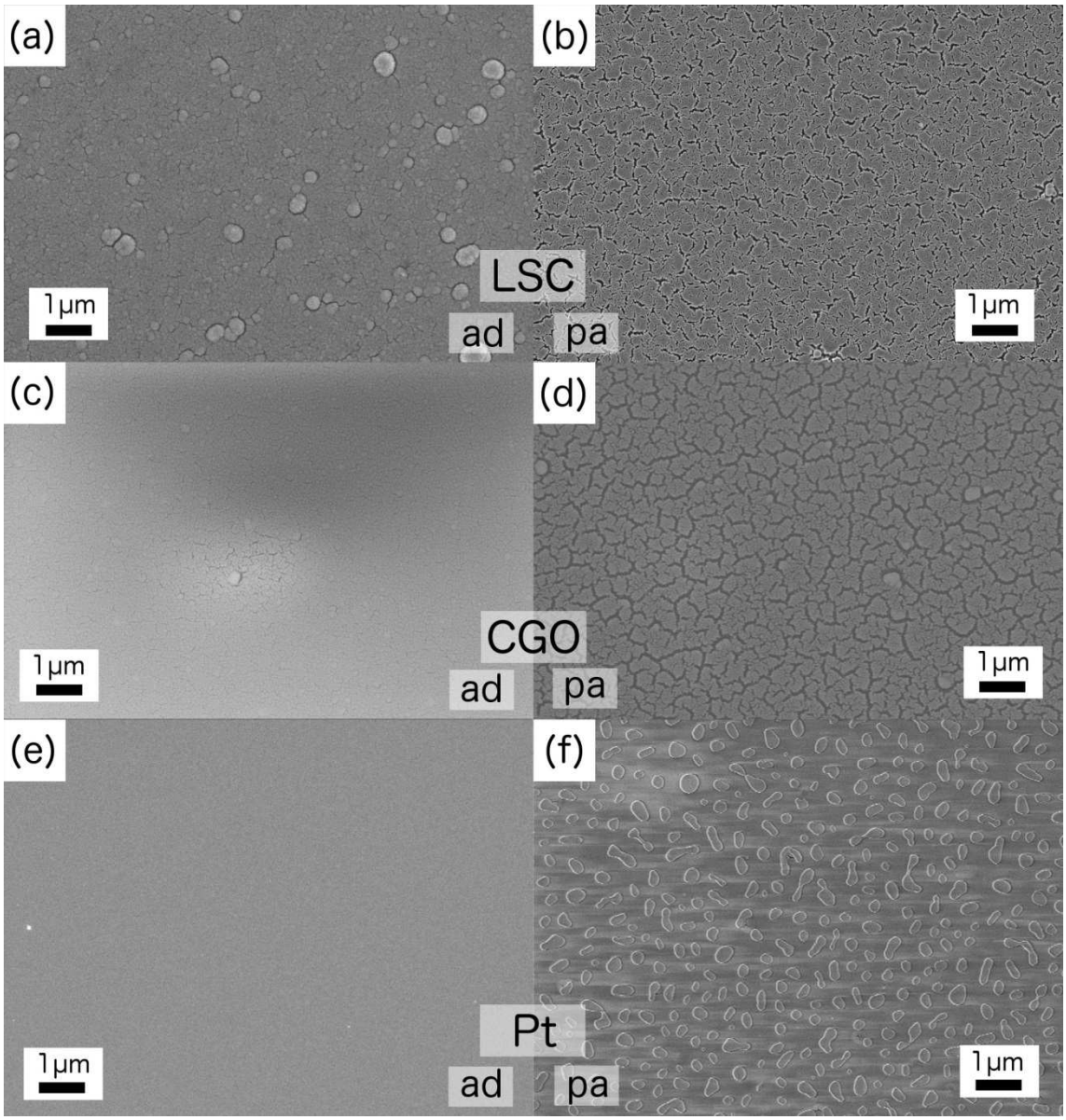

Fig. S9 Top view SEM images of the different electrodes fabricated in this work as-deposited (a, c, e - label *ad*) and post-annealed (b, d, f - label *pa*) at 700ºC.